

# Characteristics Analysis and Modeling of Train-to-Train Wireless Channel in Station Scenario

YINGFEI LIU,<sup>1,2</sup> LEI XIONG,<sup>1</sup> DAN FEI,<sup>1</sup> RUI LIU,<sup>2</sup> AND HABTE ENDALE LEGESSE<sup>2</sup>

<sup>1</sup>The State Key Laboratory of Advanced Rail Autonomous Operation, Beijing Jiaotong University, Beijing 100044, China.

<sup>2</sup>School of Electronic and Information Engineering, Beijing Jiaotong University, Beijing 100044, China.

Correspondence should be addressed to Lei Xiong; lxiang@bjtu.edu.cn

**ABSTRACT** In this paper, ray tracing (RT) is used to analyze the characteristics of Train-to-Train (T2T) wireless channel in 2.1 GHz frequency band, including path loss, multipath clustering, delay spread, Rice factor, angular spread and channel non-stationarity. It is found that the change of environment has a great influence on the characteristics of wireless channel, which not only causes the birth and death of multipath clusters, but also makes the channel appear non-stationary characteristics. In order to characterize the non-stationarity of T2T wireless channel, we introduce the time correlation coefficient (TPCC) of power delay profile (PDP), analyze the non-stationarity of T2T wireless channel, and give the quasi-stationarity distance. The results are basically consistent with the measured data.

**INDEX TERMS** High-speed rail, T2T, Ray-tracing, Multipath clustering and tracking, Non-stationary channel modeling

## I. INTRODUCTION

With the development of the next generation train control system, T2T communication has gradually become the focus of academic research in order to ensure the real-time and accuracy of high-speed railway mobile communication system. T2T can assist train operation control system based on Train-to-Ground (T2G) wireless communication, reduce communication delay, strengthen collision danger detection and broadcast warning, and improve train operation efficiency and safety. At the same time, T2T is also a key technology for virtual coupling and autonomous driving.

So far, the international academic research on radio wave propagation and wireless channel characteristics in railway scenarios has basically focused on the T2G wireless channel. For example, the channel models of tunnel scene [1–3], plain scene [4], viaduct scene [5–7], cutting scene [8, 9], bridge crossing scene [10] and so on are established. However, the research on T2T wireless channel is relatively few. Compared with T2I communication, T2T communication presents high dynamic characteristics of both receiver and transmitter. The rapid change of environment and scatterers in a short time makes the channel characteristics change dramatically. T2T channel is not only fast time-varying, but also non-stationary.

Given that the Multiple-Input Multiple-Output (MIMO) technology can effectively improve the channel capacity and channel reliability, and the large surface area of the train car

is easy to install the MIMO antenna system, it is possible to combine the MIMO technology with the channel spatial characterization study of T2T. A large-scale MIMO channel measurement campaign was conducted in an indoor metro environment at 3.5 GHz carrier frequency and 160 MHz bandwidth by Asad Saleem et al. The channel parameters were investigated for both co-polarization and cross-polarization. The results show that the antenna configuration and polarization type have a large impact on the channel characteristics. The angular extension changes significantly when different antenna polarizations are used on the transmit and receive antenna sides [11]. Asad Saleem et al. investigated the statistical properties of a novel geometry-based three-dimensional (3D) stochastic model for next-generation vehicle-to-vehicle (V2V) multiple-input-multiple-output (MIMO) communications in a non-isotropic scattering environment [12].

The Roll2Rail project established by the European Union in Shift2Rail is already conducting T2T wireless channel research. Paul Unterhuber et al. conducted a measurement campaign on an T2T channel traveling on two parallel tracks in an open field environment. The GSCM based on delay, doppler frequency and power output was compared with measurements in equivalent environments and scenarios. Finally, the model was qualitatively validated based on PDP and DSD and found to be in good agreement between the model and the measured data [13]. A train-to-

28  
29  
30  
31  
32  
33  
34  
35  
36  
37  
38  
39  
40  
41  
42  
43  
44  
45  
46  
47  
48  
49  
50  
51  
52  
53

54 train millimeter-wave propagation measurement campaign in  
 55 the service of virtual coupling was carried out by Mohammad  
 56 Soliman et al. The received signal power in the open area  
 57 was analyzed and modeled using a two-ray path loss model.  
 58 The results show that the received power near the platform is  
 59 higher than in the open area due to the strong contribution of  
 60 the reflected signal from the platform [14]. Erislandy Mozo  
 61 Bigñotte et al. presented six tapped delay line models for T2T  
 62 communication. The hilly terrain and train station scenarios  
 63 cover large, medium and short distances. The results show  
 64 that simulated channels using any of the proposed models  
 65 correlate with measurements made using a DLR channel  
 66 sounder. The proposed TDL model can be modeled and the  
 67 maximum number of taps equal to 16 [15]. Paul Unterhuber  
 68 and Michael Walter et al. extracted channel parameters for  
 69 train-to-train scenarios for typical environments such as train  
 70 stations, open fields and hilly terrain. Smoothness of the  
 71 channel in time and frequency is dealt with, and distance-  
 72 dependent model parameters are proposed for all random  
 73 channel parameters [16]. The César Briso-Rodríguez team  
 74 conducted T2T channel measurements and modeling in the  
 75 900 MHz and 2400 MHz frequency bands of the Madrid  
 76 Metro tunnel scenarios [17]. It is found that for straight  
 77 tunnels, the path loss factor  $n$  is 1.139 (900 MHz band) and  
 78 1.071 (2400 MHz band), respectively, for curved tunnels,  
 79 the path loss model is a piecewise function. Ke Guan from  
 80 Beijing Jiaotong University and others developed channel  
 81 measurement equipment based on UWB (UltraWide Band)  
 82 technology, conducted channel measurements on the tera-  
 83 hertz frequency band T2T channel, extracted channel char-  
 84 acteristics, and physically explained the channel characteristics  
 85 using self-developed RT technology [18].

86 Most of the existing literature is about channel mea-  
 87 surements for scenarios such as highways, cities and sub-  
 88 urbs, which involve communication between two vehicles.  
 89 For high-speed railway scenarios, the cost of channel mea-  
 90 surements is high and the feasibility of implementation is  
 91 low, and few of the existing studies have investigated the  
 92 channel of T2T. Therefore, in this paper, we adopt RT tech-  
 93 nique, which is less costly, less time-consuming and easier  
 94 to implement, to establish a three-dimensional radio wave  
 95 propagation scenario model to analyze and study the radio  
 96 wave propagation and channel characteristics of T2T. Due  
 97 to the high-speed movement of the double ends of the train,  
 98 the changes in the scenario within a short period of time  
 99 will cause drastic changes in the channel characteristics,  
 100 and the challenge of channel non-stationary brought by T2T  
 101 communication needs to be paid more attention to. Mean-  
 102 while, in T2T scenarios, the collection of scatterers in the  
 103 surrounding makes the multipath signals arrive in the form  
 104 of clusters, however, due to the rapid change of scatterers  
 105 in the environment, significant multipath birth and death  
 106 phenomena will occur. Studying the environmental factors  
 107 affecting the multipath components and clustering the MPCs  
 108 to further investigate the multipath cluster birth and death  
 109 process can more accurately reflect the propagation of the

110 signal in the environment and establish the channel model.  
 111 Therefore, it is necessary to analyze the characteristics of  
 112 T2T wireless channel, which lays a foundation for the design  
 113 of communication system and train control system.

114 The station is an important scenario of high-speed  
 115 railway, and also a very complex scenario of radio wave  
 116 propagation. Therefore, this paper mainly focuses on the  
 117 station communication scenario, and uses RT technology to  
 118 analyze the radio wave propagation mechanism and wireless  
 119 channel characteristics between high-speed trains under the  
 120 target frequency band of 5G-R selected by China National  
 121 Railway Group (2.1 GHz). The time-varying non-stationary  
 122 characteristics and dynamic multi-path clustering character-  
 123 istics of T2T wireless channel are emphatically studied, and  
 124 the time-varying non-stationary channel model is established,  
 125 it provides reference for T2T communication system optimi-  
 126 zation.

127 The rest of the paper is arranged as follows: section  
 128 II, which makes 3D modeling of high-speed train and sta-  
 129 tion scenarios, introduces the ray-tracing technology and the  
 130 parameters of simulation configuration, in section III, the  
 131 channel data obtained from RT simulation are processed,  
 132 the channel characteristics are extracted, and the multipath  
 133 clustering and time-varying non-stationary characteristics are  
 134 analyzed and modeled, section IV summarizes channel char-  
 135 acteristics and gives recommendations.

## II. THREE-DIMENSIONAL SCENARIO MODELING

### A. THE TRAIN MODEL

136 According to CRH380AL train, the high-speed train  
 137 model is established. CRH380AL train adopts 8-section and  
 138 16-section marshalling. In order to reduce the complexity of  
 139 the model and the operational difficulty of the simulation  
 140 without affecting the simulation results, the 8-section mar-  
 141 shalling train model is established in this paper, as shown in  
 142 Figure 1. The train is 201.50 m long, 3.38 m wide and 3.70  
 143 m high.

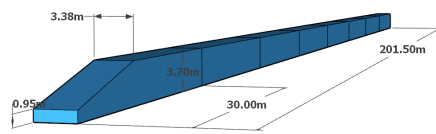


**FIGURE 1.** Train model: The black mark represents the size data of the train.

### B. SCENARIO MODELS

147 This paper refers to Tianmen North Station in Hubei  
 148 Province for station scenario modeling. The station has a  
 149 scale of 2 sets and 6 tracks (2 main tracks, 4 arrival and depar-  
 150 ture tracks), the effective length of the arrival and departure  
 151 tracks is 650 m, and there are 2 middle island platforms of  
 152 450 m × 12 m × 1.25 m. The platform houses and platforms  
 153 are arranged in equal length, among which track 1, 2, 5 and  
 154 6 are arrival and departure tracks, and track 3 and 4 are

155 main tracks. The 3D model diagram of the station scenario  
156 is shown in Figure 2.

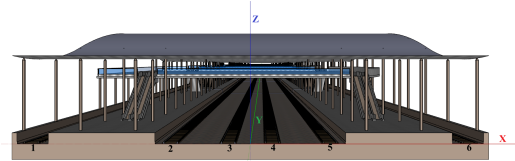


**FIGURE 2.** Station scenario model: The graphical annotations include the selection of axes and the distribution of each track.

157 In the station scenario, take the track direction as the  
158 Y axis (green coordinate axis), the horizontal plane perpen-  
159 dicular to the track direction as the X axis (red coordinate  
160 axis), the vertical to the ground direction as the Z axis (blue  
161 coordinate axis), and take the ground sideline center as the  
162 coordinate origin to establish the corresponding rectangular  
163 coordinate system. According to the principle of radio wave  
164 propagation and the research scope of the scenario, it is  
165 analyzed that the influence of rail, track and inner fence  
166 on ray propagation can be ignored. Therefore, in order to  
167 reduce the calculation amount of RT, the scenario model is  
168 simplified, and some curved models such as columns and  
169 elevators are simplified to plane models.

### C. RAY TRACING SIMULATION AND PARAMETER SETTING

170 RT is an electromagnetic environment prediction  
171 method based on geometric optics (GO) theory and uniform  
172 diffraction theory (UTD). The basic principle is to simplify  
173 electromagnetic wave propagation as a ray model while  
174 considering optical mechanisms such as direct, reflection,  
175 scattering, diffraction and transmission. By tracking each  
176 ray that reaches the receiving antenna within the scenario,  
177 it can describe the propagation path of radio waves through  
178 rays in optical theory under the condition that the scenario  
179 information is known, so as to obtain the multipath geometric  
180 parameters necessary for calculating electromagnetic char-  
181 acteristics, including ray power, delay, arrival angle, departure  
182 angle, etc. It has very broad application prospects both in  
183 doors and outdoors, such as stations, tunnels, and viaducts.

184 RT is one of the deterministic modeling methods, which  
185 depicts the dynamic changes in channel state by setting snap-  
186 shots at different positions. Therefore, the channel on each  
187 snapshot is static, and each snapshot can be used as a time  
188 slice. The following expressions about channel parameters  
189 will be expressed on the basis of snapshots.

190 The simulation sets two trains (T1 and T2) on tracks  
191 4 and 5 respectively, with T1 passing at a speed of 350  
192 km/h and T2 remaining stationary. After preliminary sim-  
193 ulation analysis, it was found that the impact of diffraction  
194 on the wireless channel can be ignored, so the radio wave  
195 propagation mechanism only considers Line-of-Sight (LoS),  
196 reflection, and scattering. To balance the complexity and  
197 accuracy of the simulation, the reflection order is set to 2.  
198 This article assumes T1 as the transmitter and T2 as the

199 receiver, and sets 631 snapshots at 1 m intervals. T1 and  
200 T2 both use omnidirectional antennas with an antenna gain  
201 of 8 dB, which are installed in the center of the top of the  
202 headstock. The RT parameters are shown in Table 1.

**TABLE 1.** RT parameter table

Parameter	Value
Frequency band [GHz]	2.1
Bandwidth [MHz]	100
Resolution [MHz]	1
Propagation mechanisms	LoS, reflection, scattering
Reflection order	2
Scattering mode	DirectiveMode
Type of train antenna	Horizontal omnidirectional antenna
Antenna gain [dB]	8
Antenna position of T1	(2.5, 620:-2:0, 4.11)
Antenna position of T2	(9, 401.75, 4.11)
Train speed $v$ [km/h]	350
Snapshot spacing $d_s$ [m]	1

203 The coordinate system of the simulation is calculated  
204 from the ground surface of the station, 4.11 m not only  
205 includes the height of the train and the antenna, but also  
206 includes the height of the railway track and the trackless  
207 bed, which is a total of 0.31 m, so the height of the antenna  
208 is 10cm. The interval between snapshots is only 1m, and  
209 it has been found that this does not improve the accuracy  
210 of the simulation results significantly and seriously affects  
211 the efficiency of the simulation by setting smaller intervals  
212 between snapshots during the simulation.

### III. ANALYSIS AND MODELING OF WIRELESS CHANNEL CHARACTERISTICS

213 Channel transfer function (CTF) and ray parameters can  
214 be obtained by RT simulation, where the rays parameters  
215 include electric field strength, time delays, and angles, etc.  
216 Thus, the most preliminary ray-based channel impulse re-  
217 sponse (CIR) model can be obtained as Equation (1), where  
218  $N$  represents the number of rays,  $\tau_n$ ,  $\omega_n$ ,  $\psi_n$  respectively are  
219 the time delay, angle of arrival (AoA) and angle of departure  
220 (AoD) of the  $n_{th}$  ray,  $\beta_n$  is the complex amplitude of the  
221  $n_{th}$  ray, and  $\chi_n$  is the phase of the ray, which is a statisti-  
222 cally independent random variable uniformly distributed over  
223  $[0, 2\pi]$ .

$$h(t, \Theta_{\text{AoA}}, \Theta_{\text{AoD}}) = \sum_{n=1}^N \beta_n e^{j\chi_n} \delta(t - \tau_n) * \delta(\Theta_{\text{AoA}} - \omega_n) * \delta(\Theta_{\text{AoD}} - \psi_n). \quad (1)$$

224 Next, the channel parameters can be extracted by data pro-  
225 cessing, including PDP, Rice factor  $K$ , angular spread, etc.

#### A. PROPAGATION PATH

226 Figure 3 shows the radio wave propagation path diagram  
227 at snapshot 100, 200, 300, 400, 500, 600, etc. At these  
228 locations, there are LOS paths, as well as reflection paths and  
229 scattering paths from the left and right platform pillars. When  
230 T1 approaches T2 (from snapshot 100 to snapshot 400), the  
231 number of rays gradually increases, and the number of rays  
232

is highest when T1 and T2 are closest (i.e., at snapshot 400). As T1 moves away from T2 (from snapshot 400 to snapshot 600), the number of rays gradually decreases, and the ray propagation characteristics are roughly symmetric, centered around snapshot 400.

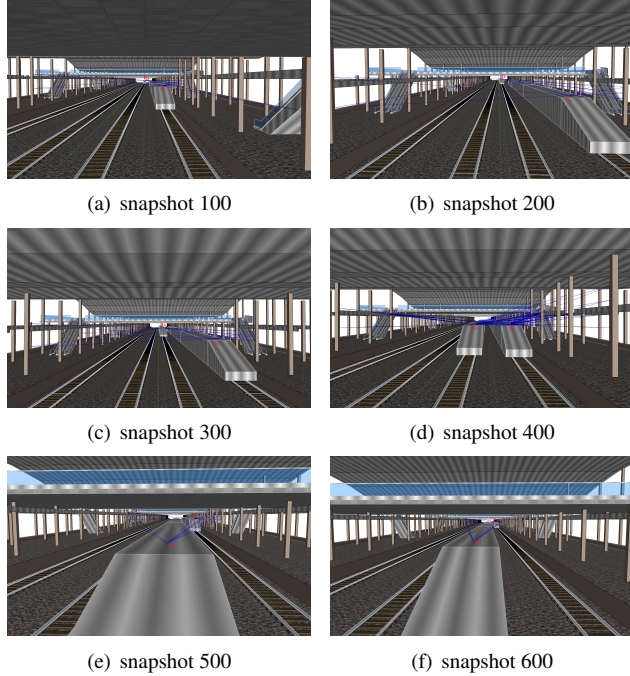


**FIGURE 3.** Propagation path at typical snapshots: The red markings represent the transmitter and receiver antenna positions, and the blue lines represent the ray propagation paths.

Since the antenna used is a horizontal omni-directional antenna with a weak effect of signals reflected from the ceiling, the ray tracing only displays rays that are within the power threshold, and rays with weaker power are not displayed. At a bandwidth of 100 MHz, the rays are difficult to distinguish in the time delay domain, but the high angular resolution of ray tracing allows the rays to be distinguished in the angular domain.

## B. PATH LOSS

Path loss refers to the loss of the received power relative to the transmitted power when the radio wave propagates. The path loss calculation formula based on RT simulation data is as follows:

$$PL(d) = \frac{N}{\sum_N |H_s(f)|^2}, \quad (2)$$

where  $H_s(f)$  represents CTF at the  $s_{th}$  snapshot,  $N$  represents the number of the frequency points in the RT simulation, and  $d$  represents the distance from the transmitter at the  $s_{th}$  snapshot.

Theory and test data show that path loss usually increases logarithmically with distance. In addition, due to the difference of the surrounding environment in different

locations, the shadow fading will occur randomly, and the free intercept path loss model is usually used:

$$PL(d) = A + 10n \lg(d) + X_\sigma, \quad (3)$$

where  $n$  is the path loss factor, indicating the rate at which the path loss increases with distance;  $d$  is the transmit-receive distance,  $A$  is the intercept, and  $X_\sigma$  represents shadow fading.

Figure 4 is the path loss data and its fitting graph. Logarithmic coordinate axis is used in the X-axis. It can be seen from the figure that the model has a good fitting effect. Figure 5 is the probability density function (PDF)

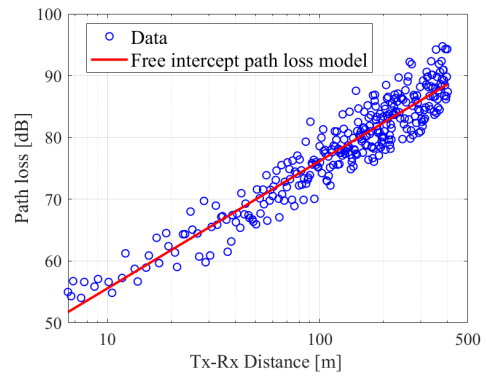


**FIGURE 4.** The blue dots represent the path loss obtained through RT simulation. The solid red line is the fitting result of the free intercept path loss model shown in the Equation (3)

distribution of the dB value of shadow fading. Currently, lognormal distribution is widely used to describe shadow fading. Its PDF is:

$$f(x) = \frac{1}{\sqrt{2\pi}\sigma} \exp\left(-\frac{(x-\mu)^2}{2\sigma^2}\right), \quad (4)$$

where  $\mu$  represents expectation and  $\sigma$  represents standard deviation.

The fitting parameters of the model are given in table 2. The free intercept path loss model indicates that the intercept  $A$  and the path loss factor  $n$  change with the environment. The results show that the path loss factor ( $n=1.6$ ) in this scenario is smaller than that in the free space path loss factor ( $n=2$ ), indicating that the scenario of the high-speed railway station is relatively empty and semi-hermetic, the receiver-transmitter antennas are at the same height, and the LOS path propagation between vehicles is not obstructed. In addition to the LOS path, there are also high-power reflection and scattering paths, which increase the received power. Therefore, the path loss factor is less than  $n$  in free space. At the same time,  $A$  in this formula can be regarded as the combined effect of 32.4 and the mean value of shadow fading, the mean value of shadowing fading doesn't conclude the  $\mu$  which is fitted using the lognormal distribution. So the extra 5 dB can reflect that shadow fading still has a strong positive feedback effect on path loss.

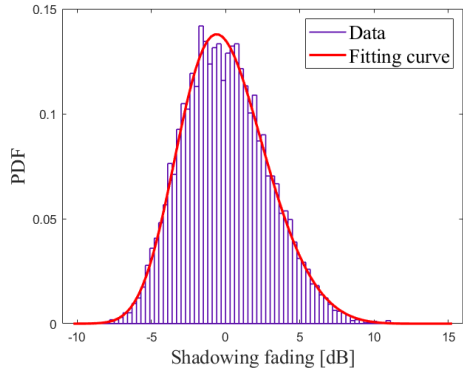


**FIGURE 5.** The blue bars represent the shadowing fading obtained through RT simulation. The solid red line is the fitting result of the shadowing fading with the Equation (4).

**TABLE 2.** Free intercept path loss model fitting parameters

Parameter	Value
$A[\text{dB}]$	37.38
$n$	1.96
$\mu[\text{dB}]$	-0.72
$\sigma[\text{dB}]$	2.89

### C. PDP

PDP represents the spectrum formed by the expected value of the received signal power at a certain time delay, reflecting the distribution of multipath power at different time delays. In this paper, the channel at each snapshot obtained by RT simulation can be considered static, and PDP is extracted based on CIR at each snapshot, as follows:

$$P_s(\tau) = |h_s(\tau)|^2, \\ h_s(\tau) = \int_{-\infty}^{\infty} H_s(f) e^{j2\pi f\tau} df, \quad (5)$$

where  $s$  represents the snapshot index,  $P_s(\tau)$  presents PDP at the  $s$ th snapshot,  $h_s(\tau)$  is CIR at the  $s$ th snapshot.

The PDP at each snapshot is shown in Figure 6. We use the multipath component with the smallest delay  $\tau$  as the normalization criterion. In this scenario, LOS path always exists, so the power is strongest at 0 ns. The power here is in dB, which is for the channel. ‘dB’ stands for a gain or loss. It represents the loss propagated solely by the channel path, not including the power of the transmitting antenna as well as the antenna gain. The PDP at different snapshot locations is significantly different, and the channel presents obvious non-stationary characteristics. The following rules can be found:

- 1) At the low delay of less than 100 ns, the high power multipaths appear at many snapshots, which is caused by the reflection and scattering effect of evenly and densely distributed pillars on both sides of the station.
- 2) As can be seen from the blue marked part of the Figure 6, when the transmit-receive antenna distance is greater than 100 m, that is, snapshot 1 to snapshot 300, there are a lot of multipaths with relatively stable delay at 140 ns and

340 ns, this is caused by the reflection and scattering of the left column (closest to track 2) and the right column (closest to track 5) of the station respectively; there are multipaths at snapshot 500 to snapshot 631 with a delay of 370 ns, it is caused by the reflection and scattering from the column on the right side of the platform.

- 3) When the transmit-receive antenna distance is less than 100 m, that is, snapshot 300 to snapshot 500, the number of multipaths is large and the delay changes dramatically, which is caused by the simultaneous reflection and scattering of pillars on both sides of the platform.

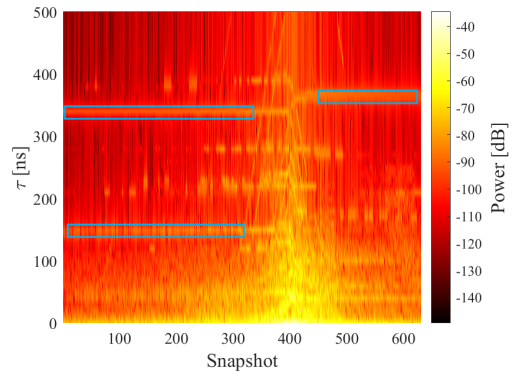


**FIGURE 6.** The PDPs of all snapshots: The x-axis represents the different snapshots, the y-axis represents the delay, and the colors represent the gain of the propagation paths.

### D. MULTIPATH CLUSTERING AND TRACKING

In actual channels, multipath components (MPCs) often appear in clusters [19–21]. A cluster is defined as a set of MPCs with similar delay, arrival Angle and departure Angle at the same time. Cluster parameters usually remain unchanged for a period of time, which can reflect channel characteristics more accurately, especially suitable for non-stationary channel modeling. Therefore, the identification and modeling of clusters is an important aspect of current channel research.

From PDP shown in Figure 6, it can be seen that there are obvious non-stationary and MPCs clustering phenomena in T2T channel in this paper. Based on the channel data obtained by RT, this paper adopts clustering and tracking algorithm to complete the modeling of clusters in time-varying non-stationary channels. The flow chart is shown in Figure 7.

- Firstly, the KPowerMeans algorithm is used to cluster the MPCs under each snapshot [22], and the centroidids of the clusters under each snapshot and the MPCs parameters within the clusters (power, delay, azimuth angle and elevation angle of arrival and departure angle) are obtained.
- Clusters of different snapshot have birth and death phenomena, including birth, death and inheritance of clusters. The tracking algorithm [23, 24] based on Multipath Component Distance (MCD) is used to judge the

322  
323  
324  
325  
326  
327  
328  
329  
330  
331  
332

333  
334  
335  
336  
337  
338  
339  
340  
341  
342  
343  
344  
345  
346  
347  
348  
349  
350  
351  
352  
353  
354  
355  
356  
357  
358  
359

birth and death states of clusters at different snapshots, track the changes of clusters, and obtain time-varying clusters.

- Finally, according to the results of clustering and tracking, the inter-cluster parameters and intra-cluster parameters of clusters are extracted to complete the modeling of clusters.

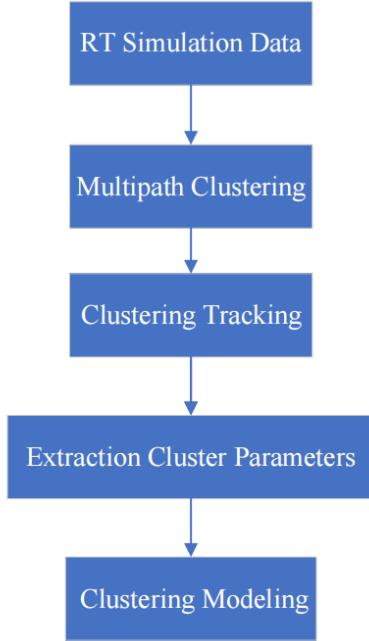


**FIGURE 7.** The flow chart of clustering and tracking: The above process represents the first step of the flowchart, and the second half of the subsection continues with steps 2-5.

---

#### Pseudo-code 1: Multipath Clustering Framework

---

```

1 for  $K = K_{\min}, \dots, K_{\max}$  do
2   Plan  $K$  clusters for the specified snapshot:
3    $R_K = \text{KPowerMeans}(P, X, K)$ 
4   Validate  $K$  clusters:
5    $v_K = \text{CombinedValidate}(R_K)$ 
6 end
7 Find optimum number of clusters:
8  $K_{\text{opt}} = \arg \max_K v_K, R_{\text{opt}} = R_{K_{\text{opt}}}$ 
9 Prune optimum number cluster set:
10  $R^p = \text{ShapePrune}(R_{\text{opt}})$ 
  
```

---

2) KPowerMeans

Based on KMeans algorithm, KPowerMeans algorithm considers the influence of power when calculating the distance of adjacent multipaths. The input parameters are the parameter matrix  $X = [x_1, \dots, x_L]$  of all  $L$  MPCs and the power matrix  $P = [P_1, \dots, P_L]$ , the parameter vector  $x_l$  of each MPCs contains delay  $\tau$ , AoA's azimuth angle and elevation angle  $(\phi_{\text{AoA}}, \theta_{\text{AoA}})$ , AoD's azimuth angle and elevation angle  $(\phi_{\text{AoD}}, \theta_{\text{AoD}})$ .

For the specified  $K$  clusters, the algorithm randomly selects  $K$  initial cluster centorids  $c_1^{(0)}, c_K^{(0)}$ , within the given maximum number of MaxIterations, first use the MCD algorithm to find the closest cluster centorid to each MPC and store its corresponding cluster index in  $I^{(i)}$ , then go through the indice of all MPCs cluster centorids. The set  $C^{(i)}$  of MPCs under each cluster centorid is obtained, and then the MCD algorithm is used to calculate the new cluster centorid  $c_k^{(i)}$  of MPCs under each cluster centorid  $c_k^{(i-1)}$  again, until all the calculated new cluster centorids are the same as the last iteration, then the iteration process exits and the set  $R_K$  is returned. See Pseudo-code 2 for details.

KPowerMeans algorithm uses MCD to calculate the distance between MPC ( $c_i$ ) and cluster centorid ( $c_j$ ). MCD calculates the angle and delay differently, such as Equation (6) and Equation (7), where  $\theta_i$  represents the azimuth angle.  $\varphi_i$  represents the elevation angle,  $\tau_i$  represents the delay,  $\tau_{\text{std}}$  represents the standard deviation of the delay of all MPCs,  $\zeta$  is the delay scale factor, reflecting the importance of the time domain, in general,  $\zeta = 1$ . Equation (8) gives the MCD distance considering angle and delay.

$$\text{MCD}_{\text{AoA/AoD}}(c_i, c_j) = \frac{1}{2} \left| \begin{pmatrix} \sin(\theta_i) \cos(\varphi_i) \\ \sin(\theta_i) \sin(\varphi_i) \\ \cos(\theta_i) \end{pmatrix} - \begin{pmatrix} \sin(\theta_j) \cos(\varphi_j) \\ \sin(\theta_j) \sin(\varphi_j) \\ \cos(\theta_j) \end{pmatrix} \right| \quad (6)$$

$$\text{MCD}_\tau(c_i, c_j) = \zeta \cdot \frac{|\tau_i - \tau_j|}{\Delta\tau_{\max}} \cdot \frac{\tau_{\text{std}}}{\Delta\tau_{\max}}, \quad (7)$$

$$\Delta\tau_{\max} = \max_{i,j} \{|\tau_i - \tau_j|\},$$

---

**Pseudo-code 2: KPowerMeans Algorithm**


---

```

1 Randomly choose  $K$  initial centroids  $c_1^{(0)}, \dots, c_K^{(0)}$ 
2 for  $i = 1, \dots, \text{MaxIterations}$  do
3   Assign MPCs to cluster centroids and store
      indices:
4   for  $l = 1, \dots, L$  do
5      $I_l^{(i)} = \arg \min_k \{P_l \cdot \text{MCD}(x_l, c_k^{(i-1)})\}$ 
6   end
7    $I^{(i)} = [I_1^{(i)}, \dots, I_L^{(i)}]$ ,
8   for  $k = 1, \dots, K$  do
9      $C_k^{(i)} = \text{Indice}_l(I_l^{(i)} = k)$ 
10  end
11   $C^{(i)} = [C_1^{(i)}, \dots, C_K^{(i)}]$ 
12  Recalculate cluster centroids  $c_k^{(i)}$  from the
      allocated MPCs to coincide with the clusters'
      centroids:
13  for  $k = 1, \dots, K$  do
14     $c_k^{(i)} = \frac{\sum_{j \in C_k^{(i)}} P_j \cdot x_j}{\sum_{j \in C_k^{(i)}} P_j}$ 
15  end
16  if  $c_k^{(i)} = c_k^{(i-1)}$  for all  $k = 1, \dots, K$  then
17    Return  $R_K = [I^{(i)}, C^{(i)}]$ 
18  end
19 end

```

---

$$\text{MCD}(c_i, c_j) = \sqrt{\|\text{MCD}_{\text{AoA},ij}\|^2 + \|\text{MCD}_{\text{AoD},ij}\|^2 + \text{MCD}_{\tau,ij}^2} \quad (8)$$

417 3) CombinedValidate

418 For the validation of clustering performance, CH index  
419 and DB index are combined in this paper. The CH index is  
420 calculated as follows:

$$\text{CH}(K) = \frac{\text{tr}(\mathbf{B}) \cdot (L - K)}{\text{tr}(\mathbf{W}) \cdot (K - 1)}, \quad (9)$$

421 where  $\text{tr}(\cdot)$  is the rank of the matrix, the matrix  $\mathbf{B}$  and  $\mathbf{W}$   
422 represent the inter-cluster scattering matrix and the intra-  
423 cluster scattering matrix respectively, and the distance is  
424 calculated using MCD algorithm.  $\text{tr}(\mathbf{B})$  and  $\text{tr}(\mathbf{W})$  can be  
425 calculated respectively as follows:

$$\begin{aligned} \text{tr}(\mathbf{B}) &= \sum_{k=1}^K L_k \cdot \text{MCD}^2(c_k, \bar{c}), \\ \text{tr}(\mathbf{W}) &= \sum_{k=1}^K \sum_{j \in C_k} \text{MCD}^2(x_j, c_k), \end{aligned} \quad (10)$$

here  $L_k$  represents the number of MPCs in the  $k_{th}$  cluster,  
426 and  $\bar{c}$  represents the global cluster centroid of all MPCs:  
427

$$\bar{c} = \frac{\sum_{l=1}^L P_l \cdot x_l}{\sum_{l=1}^L P_l}. \quad (11)$$

The DB index is calculated as follows:

$$\text{DB}(K) = \frac{1}{K} \sum_{i=1}^K R_i, \quad (12)$$

where  $R_i$  is a function that describes the intra-cluster compactness  $S_k$  and the inter-cluster dispersion  $d_{ij}$ , as follows:

$$\begin{aligned} R_i &= \max_{\substack{j=1, \dots, K \\ j \neq i}} \left\{ \frac{S_i + S_j}{d_{ij}} \right\}, \\ S_k &= \frac{1}{L_k} \sum_{l \in C_k} \text{MCD}(x_l, c_k), \\ d_{ij} &= \text{MCD}(c_i, c_j). \end{aligned} \quad (13)$$

In the combination of the two validation criteria introduced, this paper uses the minimum value in the DB index to restrict the set of optimal clusters to be selected. The CH index is then used to determine the optimal value of the cluster number in the set. Consider here the set of the best number of clusters  $F = K_1, \dots, K_N \subseteq [K_{\min}, K_{\max}]$ ,  $K_i$  need to satisfy:

$$\text{DB}(K_i) \leq 2 \cdot \min_K \{\text{DB}(K)\}. \quad (14)$$

The optimal number of cluster  $K_{\text{opt}}$  is the value of  $K$  corresponding to the maximum CH index in the set:

$$K_{\text{opt}} = \arg \max_{K \in F} \{\text{CH}(K)\}. \quad (15)$$

4) ShapePrune

After the optimal cluster number is determined successfully, this paper uses the clustering pruning algorithm to remove the outliers. It is mainly achieved by deleting the data points with the largest distance from the cluster centroids, and the original power and shape of the clusters are restricted by the change of the power and the parameters of the clusters within a certain range, as shown in Pseudo-code 3.

First, the optimal cluster after clustering verification is initialized as the cluster to be pruned. For each cluster, the MPCs power and the cluster power  $P_k^{(0)}$  are recorded, and the RMS delay spread and angular spread are recorded as the extension vector  $S_k^{(0)}$ . Here using  $s$  and  $k$  as the threshold factors respectively, role in the initial cluster power  $P_k^{(0)}$  and  $S_k^{(0)}$ . When the current cluster power  $P_k^{(\text{cur})}$  and extension vector  $S_k^{(\text{cur})}$  is greater than the given threshold power and extended threshold, based on MCD, the MPC farthest from the current cluster centroid is found and removed, then the current cluster power and expansion vector are recalculated until the threshold limit is not met, and the set of cluster centorids and cluster indexes of all MPCs  $R^{(p)}$  is returned.

---

**Pseudo-code 3:** ShapePrune Algorithm

---

```

1 Initialize the pruning set as an optimal clustering:
2    $R^{(p)} = R_{\text{opt}}$ 
3 for  $k = 1, \dots, K_{\text{opt}}$  do
4   Retain the initial power and parameters of the  $k$ th
    cluster:
5    $P_k^{(0)} = \sum_{j \in C_k} P_j,$ 
6    $S_k^{(0)} = [\sigma_\tau, \sigma_{\varphi_{\text{AoA}}}, \sigma_{\varphi_{\text{AoD}}}, \sigma_{\theta_{\text{AoA}}}, \sigma_{\theta_{\text{AoD}}}]^T,$ 
7   while  $P_k^{(\text{cur})} > p \cdot P_k^{(0)}$  And  $S_k^{(\text{cur})} > s \cdot S_k^{(0)}$  do
8     Find MPC with largest distance to current
     centroids  $c_k$ ;
9     Remove MPC from  $R^{(p)}$ ;
10    Recalculate  $P_k^{(\text{cur})}$  and  $S_k^{(\text{cur})}$ 
11  end
12 Restore the last deleted MPC
13 end
14 Return  $R^{(p)}$ 

```

---

**Pseudo-code 4:** Tracking Algorithm

---

```

1 for  $i = 1, \dots, M - 1$  do
2   Gets the cluster centroids of the current snapshot
     $c_k^{(i)}$  and the next snapshot  $c_k^{(i+1)}$ :
3   for  $a \in c_k^{(i)}$  do
4     Find the cluster closest to the next snapshot:
5      $b_n = \arg \min_{c \in c_k^{(i+1)}} (\text{MCD}(a, c))$ ,
6     Returns to find the cluster closest to the
     snapshot:
7      $a_n = \arg \min_{c \in c_k^{(i)}} (\text{MCD}(b_n, c))$ 
8     if  $a_n = a$  and  $\text{MCD}(a, b_n) \leq \eta$  then
9       |  $a$  and  $b_n$  can be regarded as a cluster
10      end
11    end
12  Update the set of clusters
13 end

```

---

## 461 5) Clustering Tracking

462 The tracking algorithm of cluster is based on the dis-
463 tance between cluster centorids. Because the location of
464 cluster centorids involves multidimensional parameter space
465 (angle and delay), MCD is still chosen as the distance metric.
466 Based on the clustering results obtained, clustering tracking
467 is performed by checking the MCD between cluster centorids
468 between adjacent locations, Where  $M$  represents the number
469 of snapshots. For each old cluster in the  $i_{th}$  snapshot, the
470 nearest new cluster is found in the  $(i + 1)_{th}$  snapshot. In turn,
471 the nearest old cluster is determined for this new cluster. If the
472 old cluster and the new cluster are both closest to each other
473 and the MCD between them is below the predefined threshold
474  $\eta$ , then the two clusters are related. Otherwise, unrelated old
475 clusters are considered "dead" and unrelated new clusters are
476 considered "born". See Pseudo-code 4 for details.

## 477 6) Cluster Parameters Modeling

478 According to the above processing method, KPower-
479 Means algorithm can obtain the cluster centorids and MPCs
480 information (power, delay, azimuth angle and elevation angle
481 of arrival angle and departure angle) under each snapshot,
482 and MCD-based tracking algorithm can obtain the inher-
483 itance relationship between clusters under different snap-
484 shots. Finally, the inter-cluster parameters and intra-cluster
485 parameters describing the distribution, density and shape of
486 clusters in the channel can be extracted. The inter-cluster
487 parameters include the number, the arrival time, the life cycle
488 and the power delay attenuation factor of clusters. The intra-
489 cluster parameters include the distribution and amount of
490 intra-cluster MPCs, the delay spread of the cluster, and the
491 angular spread. In this paper, the number, life cycle, arrival
492 time of clusters and the amount of intra-cluster MPCs,  $K$ 
493 factor for clusters are preliminarily modeled, and the results
494 are as follows:

495 Clusters are divided into LOS clusters and reflection and
496 scattering clusters. As shown in Figure 8, different snapshots
497 have 1-6 clusters respectively, with an average value of 2.3.
498 Figure 6 only shows the display of multipath power in time
499 delay domain. The multipath clustering used in this paper
500 not only takes into account the factors of delay and power,
501 but also the effects of arrival Angle and departure Angle.
502 Therefore, the clustering effect presented by PDP is only
503 a partial display of the clustering algorithm in time delay
504 domain.

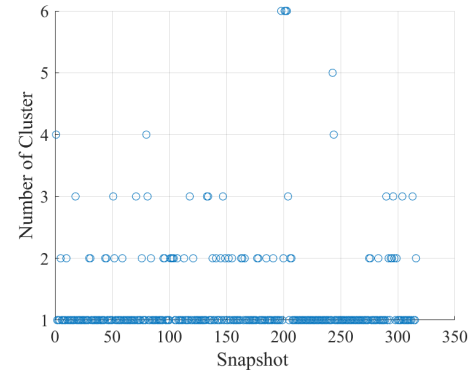


FIGURE 8. The x-axis represents the different snapshots, the y-axis represents the number of clusters for each snapshot.

505 The life cycle of a cluster is defined as the time that a
506 cluster experiences from birth snapshot  $a$  to death snapshot
507  $b$ , as follows:

$$\text{Cluster Life} = \frac{(b - a) \cdot d_s}{v}. \quad (16)$$

508 The CDF of the life cycle of the reflection and scattering
509 clusters cluster is given in Figure 9, with an average value

510 of 21.6 ms, which is about 1.05 snapshots. The longest du-  
 511 ration is 6 snapshots. The shorter the duration of the cluster,  
 512 the worse the channel stationarity. The channel will undergo  
 513 drastic changes in a short period of time, and the MPCs in  
 514 the cluster also change rapidly. This is also consistent with  
 515 many evenly spaced arrayed reflectors and scatters in the  
 516 scenario. These reflectors and scatters have a great impact on  
 517 the T2T channel and greatly reduce the survival time of the  
 518 cluster. The birth and death of the cluster is closely related  
 519 to the stationarity of the channel, which also affects the time  
 520 interval of the receiver's estimation of the channel indirectly.

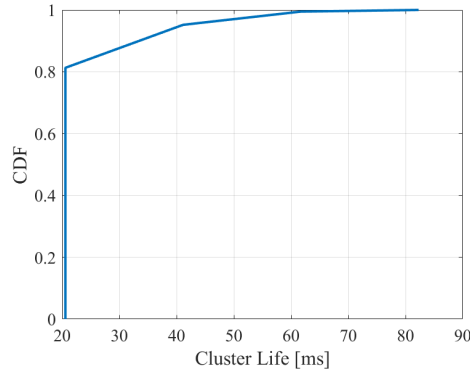


**FIGURE 9.** The solid blue line is the CDF of the cluster life.

521 Based on the life cycle of clusters, the distribution of  
 522 clusters can be accurately obtained by modeling the arrival  
 523 time of clusters. The arrival time of the cluster is defined as  
 524 the moment when the cluster is born, that is, the time from  
 525 the start of the train to the birth of the cluster. The CDF of  
 526 the arrival time of all clusters is given in Figure 10. It can  
 527 be seen that the time interval of cluster arrival time can be  
 528 approximately uniformly distributed, which means that the  
 529 clusters will appear evenly during the entire process, with  
 530 an average of 1.09 new clusters per snapshot birthing. By  
 531 converting snapshot spacing and speed into time, an average  
 532 of 54.5 clusters per second are born.

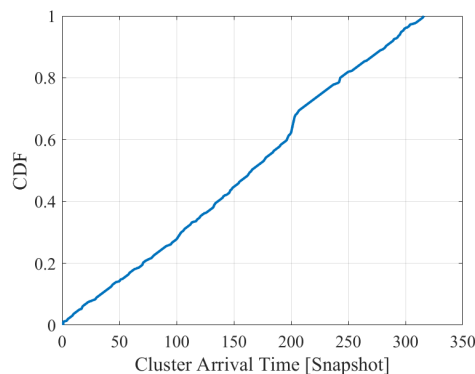


**FIGURE 10.** The solid blue line is the CDF of the cluster arrival time.

533 The amount of intra-cluster MPCs represents the num-  
 534 ber of multipaths contained inside each cluster, and the CDF

535 of the number of MPCs per cluster is given in Figure 11.  
 536 50% of the amount of intra-cluster MPCs are within 8 paths,  
 537 and the remaining can be as high as 60. The mean value of  
 538 the amount of intra-cluster MPCs in the station scenarios is  
 14.35, and the standard deviation is 15.71.

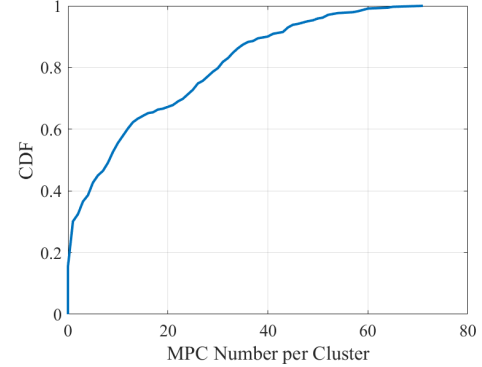


**FIGURE 11.** The solid blue line is the CDF of the amount of intra-cluster MPCs.

539 The  $K$  factor of the cluster is used to describe the power  
 540 ratio of the dominant component to the other components in  
 541 the cluster, as in Equation (17), where  $M$  represents the total  
 542 number of MPCs in the cluster,  $a_0$  represents the amplitude  
 543 of the dominant path, and  $a_m$  represents the sum of the  
 544 amplitude of the other MPCs in the cluster. The CDF of the  
 545  $K$  factor of the cluster is given in Figure 12, which shows that  
 546 the  $K$  factor of the cluster obeys the normal distribution,  
 547 and the mean of the  $K$  factor of the cluster in the station scenario  
 548 is -5.52 dB and the standard deviation is 3.37 dB.

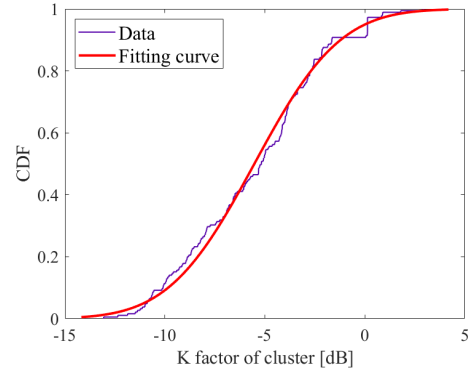


**FIGURE 12.** The blue dots represent the  $K$  factor of the cluster obtained through RT simulation. The solid red line is the fitting result of the  $K$  factor of the cluster by using normal distribution.

$$K = 10 * \log_{10} \left( \frac{|a_0|^2}{\sum_{m=1}^{M-1} |a_m|^2} \right). \quad (17)$$

549 Based on the above analysis, therefore a time-varying  
 550 dynamic cluster-based channel model is proposed on the  
 551

552 results after clustering and tracking as follows:

$$h(t, \Theta_{\text{AoA}}, \Theta_{\text{AoD}}) = \sum_{l=1}^L \sum_{k=1}^{K_l} \beta_{k,l} e^{j\chi_{k,l}} \delta(t - \tau_l - \tau_{k,l}) \times \delta(\Theta_{\text{AoA}} - \Omega_l - \omega_{k,l}) \delta(\Theta_{\text{AoD}} - \Psi_l - \psi_{k,l}), \quad (18)$$

553 where  $L$  represents the number of clusters,  $K_l$  represents the  
 554 number of rays of the  $L_{th}$  cluster,  $\tau_l$ ,  $\Omega_l$ ,  $\Psi_l$  are respectively  
 555 the time delay, AoA and AoD of the  $L_{th}$  cluster,  $\tau_{k,l}$ ,  $\omega_{k,l}$ ,  
 556  $\psi_{k,l}$  respectively are the time delay, AoA and AoD of the  $l_{th}$   
 557 cluster,  $\beta_{k,l}$  is the complex amplitude of the  $k_{th}$  ray in the  
 558  $l_{th}$  cluster, and  $\chi_{k,l}$  is the phase of the ray, which is a sta-  
 559 tistically independent random variable uniformly distributed  
 560 over  $[0, 2\pi]$ . Future work will further analyze the power and  
 561 time-space characteristics of clusters.

## E. DELAY SPREAD

562 In the wireless channel, the ray from the transmitting  
 563 antenna to the receiving antenna propagating on different  
 564 paths will lead to different delays. Large delay extension  
 565 will lead to severe inter-symbol interference (ISI), which will  
 566 cause the performance of the communication system to be  
 567 seriously degraded. Based on RT simulation data, the RMS  
 568 delay spread in this scenario is explored. Using the delay  $\tau$   
 569 of different rays and the power under this delay, the average  
 570 delay and RMS delay spread can be obtained:

$$T_m(s) = \frac{\sum_{i=1}^{n(s)} P_s(\tau_i) \tau_i}{\sum_{i=1}^{n(s)} P_s(\tau_i)}, \quad (19)$$

$$S_\tau(s) = \sqrt{\frac{\sum_{i=1}^{n(s)} P_s(\tau_i) \tau_i^2}{\sum_{i=1}^{n(s)} P_s(\tau_i)} - T_m(s)^2},$$

572 where  $n(s)$  is the number of rays at the  $s_{th}$  snapshot,  $P_s(\tau_i)$   
 573 represents the power of the  $i_{th}$  ray at the  $s_{th}$  snapshot under  
 574 the delay.  $T_m(s)$  and  $S_\tau(s)$  represent the average delay and  
 575 RMS delay spread at the  $s_{th}$  snapshot, respectively. Figure  
 576 13 shows the change of RMS delay spread with the distance  
 577 between receiver-transmitter antennas and its fitting curve.  
 578 The following rules can be found:

579 Overall, the RMS delay spread is large, with a value of  
 580 39.56 ns, which is closely related to the rich MPCs in the  
 581 station scenario. Near snapshot 400, the RMS delay spread  
 582 is the smallest, when the path loss of the LOS path between  
 583 the receiver-transmitter antennas is the smallest, and the LOS  
 584 path power is much larger than the reflection and scattering  
 585 power. In other snapshots, the reflection and scattering has  
 586 relatively larger power and larger delay spread.

587 There is a close relationship between RMS delay spread  
 588 and transmitting-receiving distance. The literature [25] de-  
 589 duces and finds out that the RMS delay spread is propor-  
 590 tional to the receiver-transmitter distance by measuring the  
 591 data of the multipath delay spread in the LOS case in an  
 592 urban environment, and at the same time, explains why  
 593 this happens. This is a very new research direction, which

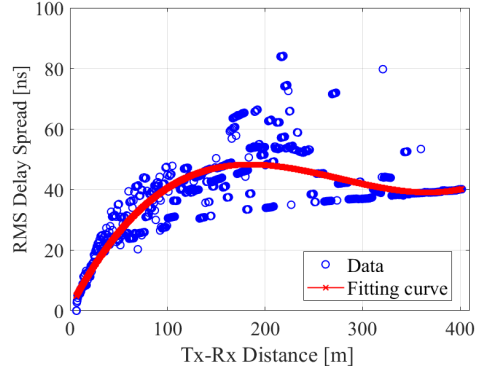


FIGURE 13. The blue dots represent the RMS delay spread obtained through RT simulation. The solid red line is the fitting result of the RMS delay spread with the Equation (20).

594 shows that wireless channel characteristics are not only path  
 595 loss affected by distance, but multipath delay spread, Rice  
 596 factor and angle spread are also correlated with the receiver-  
 597 transmitter distance, but the relationship between them in  
 598 different scenarios can not be fitted by a uniform expression,  
 599 which is different from path loss. Here, polynomial function  
 600 is used for fitting, as follows:

$$S_\tau = p_1 d^3 + p_2 d^2 + p_3 d + p_4 + X_1, \quad (20)$$

601 where  $S_\tau$  is the RMS delay spread,  $p_1$ ,  $p_2$ ,  $p_3$  and  $p_4$  are the  
 602 fitting coefficients, and  $X_1$  is the residual of the RMS delay  
 603 spread fitting. The fitting coefficients are shown in Table 3.

TABLE 3. RMS delay spread fitting coefficient and accuracy

Fitting coefficient and accuracy	Value
$p_1$	3.91
$p_2$	-11.40
$p_3$	2.84
$p_4$	48.07
RMSE	8.03

604 Other fitting effects have been tried, the fitting is still rel-  
 605 atively more consistent with the change of RMS delay spread,  
 606 the RMS delay spread presented here has a relationship with  
 607 the receiver-transmitter distance, but this relationship is not  
 608 fully deterministic, there is no uniform fixed expression.  
 609 The larger fluctuation of RMS delay spread under the same  
 610 receiver-transmitter distance also shows that the receiver-  
 611 transmitter distance is only a part of the factors affecting  
 612 its variation, and the RMS delay spread is also related to  
 613 the distribution of the surrounding reflectors, and the station  
 614 scenario is dense in scatterers, with abundant multipaths, and  
 615 there is a large amount of randomness in the RMS delay  
 616 spread, which leads to a larger RMSE.

## F. RICE FACTOR

617 The Rice factor  $K$  reflects the power ratio of the domi-  
 618 nant (or LOS) component to the other (or NLOS) component  
 619 in a snapshot. The LOS and NLOS component always exist

in this scenario, the  $|a_0|^2$  in Equation 17 can be replaced with  $P_{\text{LoS}}$  more accurately. Therefor,  $K$  can be expressed as follows [26]:

$$K (\text{dB}) = 10 \lg \frac{P_{\text{LoS}}}{P_{\text{NLoS}}}, \quad (21)$$

where  $P_{\text{LoS}}$  represents the LOS component power, and  $P_{\text{NLoS}}$  represents the reflection and scattering component power. Figure 14 shows the variation of  $K$  along with the distance between receiver-transmitter antennas and its fitting curve. The following rules can be found:

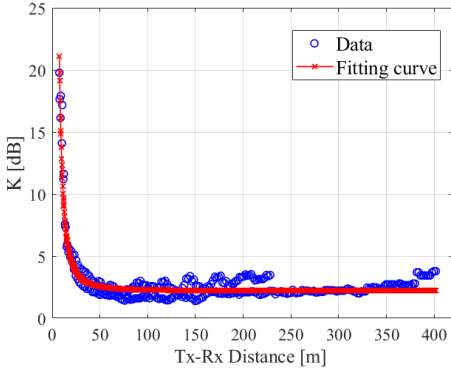


**FIGURE 14.** The blue dots represent the Rice factor  $K$  obtained through RT simulation. The solid red line is the fitting result of the Rice factor  $K$  with the Equation (22).

When the distance between receiver-transmitter antennas is less than 100 m,  $K$  changes significantly with the distance. When the receiver-transmitter antenna distance exceeds 100 m, the  $K$  remains basically unchanged at around 2.27 dB. The negative exponential distribution is used to fit the change of  $K$  with the receiver-transmitter antennas distance, and the expression is shown as follows:

$$K = a * d^b + c + X_2, \quad (22)$$

where  $a$ ,  $b$  and  $c$  are the fitting coefficients, and  $X_2$  is the fitting residual of  $K$ , whose fitting coefficients are shown in Table 4.

**TABLE 4.**  $K$  fitting coefficient and accuracy

Fitting coefficient and accuracy	Value
$a$	708.90
$b$	-1.96
$c$	2.27
RMSE	0.7

## G. SPACE CHARACTERISTICS-RMS ANGULAR SPREAD

The signals leave the transmitting antenna through different paths to the receiving antenna, and the angles of the reflected and scattered signals are different on different paths, which will form the angular spread of the arrival angle and the departure angle. Angular spread describes the energy and

spatial distribution characteristics of the signal as it leaves and arrives at the antenna. Taking AoA as an example, the mean value and angular spread of the azimuth angle  $\varphi$  and the elevation angle  $\theta$  of the arrival angle and the departure angle, as shown in Equation (23) :

$$\begin{aligned} \mu_\phi(s) &= \frac{\sum_{i=1}^{n(s)} \text{APS}(s, \phi_i) \phi_i}{\sum_{i=1}^{n(s)} \text{APS}(s, \phi_i)}, \\ S_\phi(s) &= \sqrt{\frac{\sum_{i=1}^{n(s)} \text{APS}(s, \phi_i) \phi_i^2}{\sum_{i=1}^{n(s)} \text{APS}(s, \phi_i)} - \mu_\phi(s)^2}, \\ \mu_\theta(s) &= \frac{\sum_{i=1}^{n(s)} \text{APS}(s, \theta_i) \theta_i}{\sum_{i=1}^{n(s)} \text{APS}(s, \theta_i)}, \\ S_\theta(s) &= \sqrt{\frac{\sum_{i=1}^{n(s)} \text{APS}(s, \theta_i) \theta_i^2}{\sum_{i=1}^{n(s)} \text{APS}(s, \theta_i)} - \mu_\theta(s)^2}, \end{aligned} \quad (23)$$

where  $n(s)$  is the number of rays at the  $s_{th}$  snapshot, APS represents the angle power spectrum,  $\mu_\phi(s)$  and  $\mu_\theta(s)$  represent the average azimuth angle and average elevation angle at the  $s_{th}$  snapshot, respectively.  $S_\phi(s)$  and  $S_\theta(s)$  represent the RMS angular spread of the azimuth and elevation angle at the  $s_{th}$  snapshot, respectively.

Figure 15 is the RMS Angular spread of each snapshot, in which ASA, ESA, ASD and ESD respectively represent the RMS angular spread of the azimuth and elevation angle of arrival, azimuth and elevation angle of departure. Table 6 gives the median values of ASA, ESA, ASD, and ESD.

- 1) As shown in Figure 15, the RMS angular spread of the azimuth is bigger, especially the azimuth angle of the departure. The ray is emitted from T1 to all sides through the reflection and scattering of the left and right columns, and finally reaches T2 in a certain angle range.
- 2) Regardless of the arrival angle or departure angle, the RMS angular spread of the elevation angle is very small, and the elevation angle of MPCs vary around  $90^\circ$ , almost parallel to the ground.
- 3) ASA and ESA change irregularly and have no relationship with receiver-transmitter antennas distance, while ASD and ESD, like the  $K$  factor, only change with the receiver-transmitter antennas distance when the distande is less than 100 m.

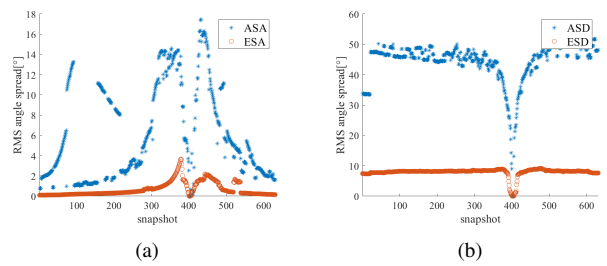


**FIGURE 15.** RMS angular spread: ASA, ESA, ASD and ESD respectively represent the RMS angular spread of the azimuth and elevation angle of arrival, azimuth and elevation angle of departure. (a) ASA and ESA of AOA for all snapshots. (b) ASD and ESD of AOD for all snapshots.

676 4) Here, the relationship between ASD, ESD and the  
 677 receiver-transmitter antennas distance is fitted by a power  
 678 approximation curve, as shown in Equation (24), where  
 679  $X_3$  is the fitting residual,  $a$ ,  $b$ ,  $c$  is the fitting coefficient,  
 680 and  $C$  is the constant. The fitting results are shown in  
 681 Figure 16. The fitting coefficients are shown in Table 5.  
 682 According to the fitted curve and formula, ASD, ESD and  
 683  $d$  are positively correlated.

$$\text{Angle\_spread} = a * d^b + c + X_3 \quad (24)$$

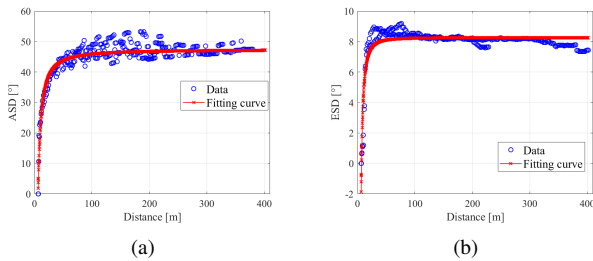


**FIGURE 16.** ASD and ESD. (a) The blue dots represent ASD obtained through RT simulation. The solid red line is the fitting result of ASD with the Equation (24). (b) The blue dots represent ESD obtained through RT simulation. The solid red line is the fitting result of ESD with the Equation (24).

**TABLE 5.** ASD and ESD fitting coefficients and accuracy

Fitting coefficient and accuracy	ASD	ESD
$a$	-467.20	-465.30
$b$	-1.24	-2.04
$c$	47.39	8.26
RMSE	3.46	0.51

**TABLE 6.** Median of RMS angular spread

Parameter	Value
ASA	4.62°
ESA	0.34°
ASD	46.16°
ESD	8.19°

## H. NON-STATIONARITY

684 There is often a relative motion between the receiver-  
 685 transmitter and the reflector-scatterer, especially in the  
 686 highly dynamic environment, the channel will show non-  
 687 stationarity, mainly in the statistical characteristics of the  
 688 channel will change with time. The existing channel model  
 689 based on WSSUS hypothesis can not accurately describe  
 690 the statistical characteristics of the channel, so it is very  
 691 important to use a reasonable method to accurately describe  
 692 the non-stationary wireless channel.

693 Channel quasi-stationary interval is an important param-  
 694 eter of the non-stationary characteristics of wireless channels,  
 695 and the characteristics of wireless channels do not change  
 696 greatly within the interval. Currently, most researches on

697 channel quasi-stationary interval are based on the analy-  
 698 sis methods of Local Scattering Function (LSF) and time-  
 699 varying coherence function [27]. The basic idea is to use the  
 700 second-order statistical characteristics of the channel to find  
 701 the correlation and difference degree of the channel.

702 For MIMO channels, Correlated Matrix Distance (CMD)  
 703 is a common method to calculate the quasi-stationary interval  
 704 [28]. By calculating the correlation matrix of the receiver or  
 705 the transmitter, the quasi-stationary interval is obtained by  
 706 using the decision threshold. For SISO channels, the Corre-  
 707 lation of Power (CP) algorithm can be used to calculate the  
 708 correlation at different sampling points [29], and the quasi-  
 709 stationary interval can be obtained by setting the threshold  
 710 decision.

711 Since the simulation is investigating a single transmitter  
 712 and single receiver station channel, the PDP at each snapshot  
 713 can be used to calculate the correlation of the channel at  
 714 different snapshots by using delay and power. In this paper,  
 715 CP algorithm is adopted, and TPCC is used as the measure of  
 716 channel stationarity. According to the definition of [30], the  
 717 TPCC of PDP in the  $s_i$  and  $s_j$  snapshots is:

$$c(s_i, s_j) = \frac{[\sum_{\tau} P(s_i, \tau)] * [\sum_{\tau} P(s_j, \tau)]}{\max \left\{ \sum_{\tau} P(s_i, \tau)^2, \sum_{\tau} P(s_j, \tau)^2 \right\}}. \quad (25)$$

718 Among them,  $P(s_i, \tau)$  is the power in  $s_i$  snapshot and  $\tau$  delay. Obviously, the value of TPCC is in the range of 0 to 1. The closer the TPCC value is to 1, the higher the channel similarity between the  $s_i$  snapshot and the  $s_j$  snapshot, and the higher the channel stationarity. The relationship between snapshot and time is used to transform, and finally Figure 719 17 is given to depict the TPCC of each moment and other 720 moments.

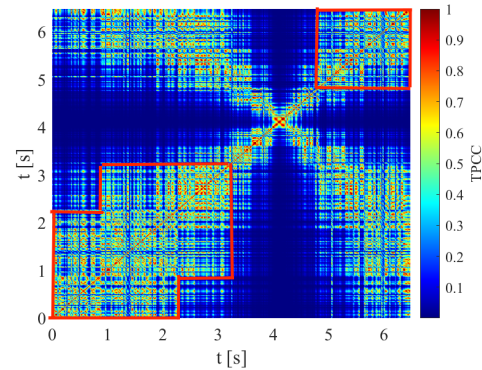


**FIGURE 17.** TPCC between every two moments: Both the x-axis and y-axis represent time, and the color represents the size of the TPCC.

721 When the receiver-transmitter antenna distance is less  
 722 than 100m (corresponding to  $t$  3.1 s-5 s), the correlation of  
 723 the channel is low, the existence of MPCs in the channel  
 724 are single and stable, and the quasi-stationary distance of  
 725 the channel is small. When the receiver-transmitter antenna  
 726 distance is greater than 100m (corresponding to  $t$  after 0 s-3 s  
 727 and 5.1 s), the channel correlation is high, the channel MPCs  
 728

734 delays change sharply, and the channel quasi-stationary dis-  
735 tance is large, as shown in the red area of Figure 17.

736 According to the threshold selection policy [31], in this  
737 scenario, the threshold is set to 0.8 to extract the quasi-  
738 stationary distance of the channel. The quasi-stationary dis-  
739 tance of the channel at each snapshot is given in Figure 18.  
740 The average quasi-stationary distance of the channel is 4.9 m,  
741 and the corresponding quasi-stationary time can be obtained  
742 as 50 ms by using the time-distance conversion formula. This  
743 is close to the measured results of [32] on the average quasi-  
744 stationary distance of vehicle-vehicle communication chan-  
745 nels and quasi-stationary time for T2T communication in  
746 [16]. The quasi-stationary time between vehicles and vehicles  
747 in the highway is 23 ms. The results are in the same order of  
748 magnitude, but the number of scatterers between vehicles and  
749 vehicles in the highway is higher than that between trains in  
750 the high-speed railway and the varieties of scatterers are rich.  
751 For example, there will be other vehicles as well as isolation  
752 zones between the vehicles and vehicles, the LOS path is  
753 not continuous, and the change of the NLOS path will be  
754 quicker and more pronounced, which will result in the quasi-  
755 stationary time to be smaller. In the reference [16], through  
756 field measurements, it was found that the stationary time  
757 of communication between the trains at the station is 65.5  
758 ms. Considering the differences in the two communication  
759 environments, the quasi-stationary time of the 50 ms channel  
760 obtained in this study is also close to it.

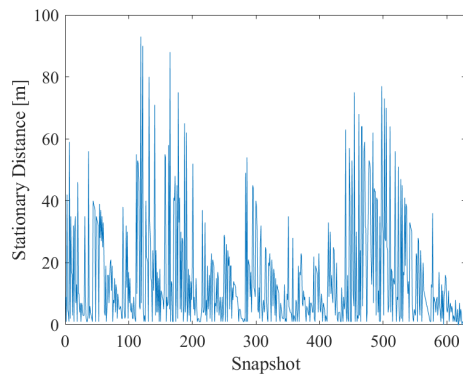


FIGURE 18. The x-axis represents the different snapshots, the y-axis represents the stationary distance for each snapshot.

761 After the analysis of channel non-stationarity, it can be  
762 drawn with the previous viaduct scenario [33] more extensive  
763 conclusions, the emergence and disappearance of MPCs,  
764 and the stationarity of the channel are closely related. The  
765 unstable change of MPCs in a short time is an important  
766 reason that leads to the decrease of the stationarity of the  
767 channel.

#### IV. CONCLUSION

768 Based on RT technology, this paper studies the char-  
769 acteristics of wireless channels between high-speed trains  
770 in the 2.1 GHz band at station scenario and establishes a  
771 channel model to provide theoretical support for T2T channel

773 research. Future work will continue to study and analyze  
774 the characteristics of the channel between two trains moving  
775 at the same time and analyze the performance of commu-  
776 nication systems such as channel capacity. The summary  
777 parameters of the channel model are shown in Table 7. The  
778 following conclusions are drawn:

- 779 • The path loss is log-linear with the distance between  
780 the receiver-transmitter antennas. The path loss factor  
781 is 1.96, and the shadow fading is more inclined to the  
782 generalized extreme value distribution.
- 783 • Multipath clustering is realized, and the number and life  
784 cycle of clusters are preliminarily quantified. Within a  
785 certain receiver-transmitter antennas distance, the RMS  
786 delay spread are polynomial distribution, and the Rice  
787 factor and angular spread of departure are power expo-  
788 nential distribution.
- 789 • When the distance between trains is relatively close,  
790 the channel correlation is low, the channel changes  
791 rapidly and violently, and the number of MPCs is large.  
792 When the distance between trains is higher, the channel  
793 correlation is bigger.
- 794 • The receiver needs to perform at least one estima-  
795 tion within a given quasi-stationary time interval (50  
796 ms), otherwise the channel estimation results will have  
797 obvious errors. This is the reason that leads to the  
798 deterioration of communication performance in high-  
799 speed railway scenarios, which needs to be considered  
800 in system design.

#### DATA AVAILABILITY

801 The data used to support the findings of this study are  
802 included within the article.

#### CONFLICTS OF INTEREST

803 The authors declare that there is no conflict of interest  
804 regarding the publication of this paper.

#### FUNDING STATEMENT

805 This work was supported by the Fundamental Re-  
806 search Funds for the Central Universities 2022JBXT001,  
807 the National Natural Science Foundation of China (Grant  
808 No.U21A20445 and No.62001135), the State Key Labora-  
809 tory of Advanced Rail Autonomous Operation under Grant  
810 RAO2023ZZ004 and RCS2022ZT013.

#### ACKNOWLEDGMENT

811 This paper mainly studies the wireless communica-  
812 tion channel characteristics of trains under the station  
813 scenario, compared with the conference to the follow-  
814 ing link: <https://ieeexplore.ieee.org/document/10065910>, al-  
815 though the research scenario and content of the paper have  
816 been changed, we would like to thank three authors (Jiadong  
817 Du, Qi Wang, Cuicui Yan) who are not on the list of authors  
818 for their preliminary work.

**TABLE 7.** Channel modeling parameters

Parameter	n	Shadow fading Mean value [dB]	Shadow fading Standard deviation [dB]	RMS delay spread Median [ns]	K Median [dB]	ASA Median [ $^{\circ}$ ]	ESA Median [ $^{\circ}$ ]	ASD Median [ $^{\circ}$ ]	ESD Median [ $^{\circ}$ ]
Value	1.96	-1.11	2.82	39.56	2.33	4.62	0.34	46.16	8.19

**REFERENCES**

- [1] A. Hrovat, G. Kandus and T. Javornik, "A Survey of Radio Propagation Modeling for Tunnels," in IEEE Communications Surveys & Tutorials, vol. 16, no. 2, pp. 658-669, Second Quarter 2014, doi: 10.1109/SURV.2013.091213.00175.
- [2] Y. Liu, A. Ghazal, C. Wang, X. Ge, Y. Yang, Y. Zhang, "Channel measurements and models for high-speed train wireless communication systems in tunnel scenarios: a survey." *Science China Information Sciences* 60 (2016): 1-17.
- [3] K. Guan, B. Ai, B. Peng, D. He, G. Li, J. Yang, Z. Zhong, T. Kürner, "Towards Realistic High-Speed Train Channels at 5G Millimeter-Wave Band—Part I: Paradigm, Significance Analysis, and Scenario Reconstruction," in IEEE Transactions on Vehicular Technology, vol. 67, no. 10, pp. 9112-9128, Oct. 2018, doi: 10.1109/TVT.2018.2865498.
- [4] C. -X. Wang, J. Bian, J. Sun, W. Zhang and M. Zhang, "A Survey of 5G Channel Measurements and Models," in IEEE Communications Surveys & Tutorials, vol. 20, no. 4, pp. 3142-3168, Fourthquarter 2018, doi: 10.1109/COMST.2018.2862141.
- [5] T. Zhou, C. Tao, S. Salous and L. Liu, "Measurements and Analysis of Angular Characteristics and Spatial Correlation for High-Speed Railway Channels," in IEEE Transactions on Intelligent Transportation Systems, vol. 19, no. 2, pp. 357-367, Feb. 2018, doi: 10.1109/TITS.2017.2681112.
- [6] X. Yin, X. Cai, X. Cheng, J. Chen and M. Tian, "Empirical Geometry-Based Random-Cluster Model for High-Speed-Train Channels in UMTS Networks," in IEEE Transactions on Intelligent Transportation Systems, vol. 16, no. 5, pp. 2850-2861, Oct. 2015, doi: 10.1109/TITS.2015.2428731.
- [7] K. Guan, B. Ai, B. Peng, D. He, G. Li, J. Yang, Z. Zhong, T. Kürner, "Towards Realistic High-Speed Train Channels at 5G Millimeter-Wave Band—Part I: Paradigm, Significance Analysis, and Scenario Reconstruction," in IEEE Transactions on Vehicular Technology, vol. 67, no. 10, pp. 9112-9128, Oct. 2018, doi: 10.1109/TVT.2018.2865498.
- [8] D. He, B. Ai, K. Guan, J. M. García-Loygorri, L. Tian, Z. Zhong, A. Hrovat, "Influence of Typical Railway Objects in a mmWave Propagation Channel," in IEEE Transactions on Vehicular Technology, vol. 67, no. 4, pp. 2880-2892, April 2018, doi: 10.1109/TVT.2017.2782268.
- [9] J. Yang, B. Ai, K. Guan, D. He, X. Lin, B. Hui, J. Kim, A. Hrovat, "A Geometry-Based Stochastic Chan-
- nel Model for the Millimeter-Wave Band in a 3GPP High-Speed Train Scenario," in IEEE Transactions on Vehicular Technology, vol. 67, no. 5, pp. 3853-3865, May 2018, doi: 10.1109/TVT.2018.2795385.
- [10] K. Guan, Z. Zhong, B. Ai and T. Kürner, "Propagation Measurements and Modeling of Crossing Bridges on High-Speed Railway at 930 MHz," in IEEE Transactions on Vehicular Technology, vol. 63, no. 2, pp. 502-517, Feb. 2014, doi: 10.1109/TVT.2013.2275912.
- [11] A. Saleem and Y. He, "Investigation of Massive MIMO Channel Spatial Characteristics for Indoor Subway Tunnel Environment," 2021 Computing, Communications and IoT Applications (ComComAp), Shenzhen, China, 2021, pp. 162-167, doi: 10.1109/ComComAp53641.2021.9652955.
- [12] A. Saleem, Y. Xu, R. A. Khan, I. Rasheed, Z. U. A. Jaffri, M. A. Layek, "Statistical Characteristics of 3D MIMO Channel Model for Vehicle-to-Vehicle Communications", Wireless Communications and Mobile Computing, vol. 2022, Article ID 9090494, 14 pages, 2022. <https://doi.org/10.1155/2022/9090494>.
- [13] P. Unterhuber, M. Walter and T. Kürner, "Geometry-Based Stochastic Channel Model for Train-to-Train Communication in Open Field Environment," 2022 16th European Conference on Antennas and Propagation (EuCAP), Madrid, Spain, 2022, pp. 1-5, doi: 10.23919/EuCAP53622.2022.9769480.
- [14] M. Soliman, P. Unterhuber, S. Sand, E. Staudinger, J. Shamshoom, C. Schindler, A. Dekorsy, "Dynamic Train-to-Train Propagation Measurements in the Millimeter Wave Band - Campaign and First Results," 2019 13th European Conference on Antennas and Propagation (EuCAP), Krakow, Poland, 2019, pp. 1-5.
- [15] E. M. Bigñote, P. Unterhuber, A. A. Gómez, S. Sand and M. M. Errasti, "Measurement Based Tapped Delay Line Model for Train-to-Train Communications," in IEEE Transactions on Vehicular Technology, vol. 72, no. 4, pp. 4168-4181, April 2023, doi: 10.1109/TVT.2022.3229142.
- [16] P. Unterhuber, M. Walter, U. -C. Fiebig and T. Kürner, "Stochastic Channel Parameters for Train-to-Train Communications," in IEEE Open Journal of Antennas and Propagation, vol. 2, pp. 778-792, 2021, doi: 10.1109/OJAP.2021.3094672.
- [17] C. Briso-Rodríguez, P. Fratilesco and Y. Xu, "Path Loss Modeling for Train-to-Train Communications in Subway Tunnels at 900/2400 MHz," in IEEE Antennas and Wireless Propagation Letters, vol. 18, no. 6, pp. 1164-1168, June 2019, doi: 10.1109/LAWP.2019.2911406.
- [18] K. Guan, B. Peng, D. He, D. Yan, B. Ai, Z. Zhong, T.

- 923 Kürner, "Channel Sounding and Ray Tracing for Train-to-Train Communications at the THz Band," 2019 13th  
 924 European Conference on Antennas and Propagation (EuCAP), Krakow, Poland, 2019, pp. 1-5.  
 925
- [19] T. Zwick, C. Fischer, D. Didascalou and W. Wiesbeck,  
 926 "A stochastic spatial channel model based on wave-  
 927 propagation modeling," in IEEE Journal on Selected  
 928 Areas in Communications, vol. 18, no. 1, pp. 6-15, Jan.  
 929 2000, doi: 10.1109/49.821698.
- [20] M. Toeltsch, J. Laurila, K. Kalliola, A. F. Molisch, P.  
 930 Vainikainen and E. Bonek, "Statistical characterization  
 931 of urban spatial radio channels," in IEEE Journal on Selected  
 932 Areas in Communications, vol. 20, no. 3, pp.  
 933 539-549, April 2002, doi: 10.1109/49.995513.
- [21] Z. Huang and X. Cheng, "A General 3D Space-  
 934 Time-Frequency Non-Stationary Model for 6G Chann-  
 935 nels," in IEEE Transactions on Wireless Communica-  
 936 tions, vol. 20, no. 1, pp. 535-548, Jan. 2021, doi:  
 937 10.1109/TWC.2020.3026356.
- [22] N. Czink, P. Cera, J. Salo, E. Bonek, J. -p. Nuutinen  
 938 and J. Ylitalo, "A Framework for Automatic  
 939 Clustering of Parametric MIMO Channel Data Includ-  
 940 ing Path Powers," IEEE Vehicular Technology Con-  
 941 ference, Montreal, QC, Canada, 2006, pp. 1-5, doi:  
 942 10.1109/VTC.2006.35.
- [23] N. Czink and C. Mecklenbrauker, "A Novel Automatic  
 943 Cluster Tracking Algorithm," 2006 IEEE 17th Interna-  
 944 tional Symposium on Personal, Indoor and Mobile  
 945 Radio Communications, Helsinki, Finland, 2006, pp. 1-  
 946 5, doi: 10.1109/PIMRC.2006.254347.
- [24] X. Cai, G. Zhang, C. Zhang, W. Fan, J. Li and  
 947 G. F. Pedersen, "Dynamic Channel Modeling for In-  
 948 door Millimeter-Wave Propagation Channels Based on  
 949 Measurements," in IEEE Transactions on Communica-  
 950 tions, vol. 68, no. 9, pp. 5878-5891, Sept. 2020, doi:  
 951 10.1109/TCOMM.2020.3001614.
- [25] J. H. Kim, Y. Yoon and Y. J. Chong, "The distance  
 952 characteristics of R.M.S. delay spread at urban low-rise  
 953 environment," 2016 International Conference on Infor-  
 954 mation and Communication Technology Convergence  
 955 (ICTC), Jeju, Korea (South), 2016, pp. 1020-1022, doi:  
 956 10.1109/ICTC.2016.7763356.
- [26] K. Mao, Q. Zhu, Y. Qiu, X. Liu, M. Song, W. Fan,  
 957 A. B. J. Kokkeler, Y. Miao, "A UAV-Aided Real-Time  
 958 Channel Sounder for Highly Dynamic Nonstationary  
 959 A2G Scenarios," in IEEE Transactions on Instrumen-  
 960 tation and Measurement, vol. 72, pp. 1-15, 2023, Art  
 961 no. 6504515, doi: 10.1109/TIM.2023.3301592.
- [27] G. Matz, "On non-WSSUS wireless fading chan-  
 962 nels," in IEEE Transactions on Wireless Communica-  
 963 tions, vol. 4, no. 5, pp. 2465-2478, Sept. 2005, doi:  
 964 10.1109/TWC.2005.853905.
- [28] M. Herdin, N. Czink, H. Ozcelik and E. Bonek,  
 965 "Correlation matrix distance, a meaningful measure  
 966 for evaluation of non-stationary MIMO channels,"  
 967 2005 IEEE 61st Vehicular Technology Conference,  
 968 Stockholm, Sweden, 2005, pp. 136-140 Vol. 1, doi:  
 969 10.1109/VETECS.2005.1543265.
- [29] B. Chen, Z. Zhong, and B. Ai, "Non-stationary channel  
 970 characteristics in high-speed railway," in 2015 IEEE  
 971 International Symposium on Antennas and Propagation  
 972 USNC/URSI National Radio Science Meeting, July  
 973 2015, pp. 97-98.
- [30] Q. Wang, D. W. Matolak and B. Ai, "Shadowing  
 974 Characterization for 5-GHz Vehicle-to-Vehicle Chan-  
 975 nels," in IEEE Transactions on Vehicular Technol-  
 976 ogy, vol. 67, no. 3, pp. 1855-1866, March 2018, doi:  
 977 10.1109/TVT.2017.2764267.
- [31] R. He, O. Renaudin, V. -M. Kolmonen, K. Haneda,  
 978 Z. Zhong, B. Ai, C. Oestges, "Characterization of  
 979 Quasi-Stationarity Regions for Vehicle-to-Vehicle Ra-  
 980 dio Channels," in IEEE Transactions on Antennas and  
 981 Propagation, vol. 63, no. 5, pp. 2237-2251, May 2015,  
 982 doi: 10.1109/TAP.2015.2402291.
- [32] A. Paier, T. Zemen, L. Bernado, G. Matz, J. Karedal,  
 983 N. Czink, C. Dumard, F. Tufvesson, A. F. Molisch,  
 984 C. F. Mecklenbrauker, "Non-WSSUS vehicular chan-  
 985 nel characterization in highway and urban scenar-  
 986 ios at 5.2GHz using the local scattering function,"  
 987 2008 International ITG Workshop on Smart An-  
 988 tennas, Darmstadt, Germany, 2008, pp. 9-15, doi:  
 989 10.1109/WSA.2008.4475530.
- [33] Y. Liu, L. Xiong, D. Fei, J. Du, Q. Wang and  
 990 C. Yan, "Characteristics for Train-to-Train Chan-  
 991 nel based on Ray Tracing," 2022 IEEE 8th Inter-  
 992 national Conference on Computer and Communica-  
 993 tions (ICCC), Chengdu, China, 2022, pp. 47-51, doi:  
 994 10.1109/ICCC56324.2022.10065910.